

# Progress in laser ultrasonics evaluation of micro- and nanoscale interfacial mechanics

Cite as: Appl. Phys. Rev. 11, 041315 (2024); doi: 10.1063/5.0220082

Submitted: 22 May 2024 · Accepted: 19 September 2024 ·

Published Online: 1 November 2024



Maroun Abi Chanem<sup>a)</sup> and Thomas Dehoux<sup>a)</sup>

## AFFILIATIONS

Université Claude Bernard Lyon 1, CNRS, Institut Lumière Matière, Villeurbanne F-69622, France

<sup>a)</sup>Authors to whom correspondence should be addressed: [maroun.abi-ghanem@univ-lyon1.fr](mailto:maroun.abi-ghanem@univ-lyon1.fr) and [thomas.dehoux@univ-lyon1.fr](mailto:thomas.dehoux@univ-lyon1.fr)

## ABSTRACT

Understanding contact mechanics and adhesion processes in thin films and micro-structured materials is fundamental in phonon and heat transport phenomena and is ubiquitous for the miniaturization of mechanical and thermal devices as well as the design/functionalization of structured surfaces and membranes. Acoustic-based methods are of great interest in this context since they provide a nondestructive mean to probe interface quality and adhesion, at various scales. In particular, Laser Ultrasonics (LU) techniques allow the generation of broadband acoustic pulses with a frequency content extending up to a few THz due to the thermoelastic expansion induced by the absorption of short laser pulses. In this review, we will explore the specificities of the LU generation/detection schemes and the unusual wide frequency range that make these opto-acoustic techniques a unique tool to study adhesion processes from micro- to nanoscales, and in a variety of systems, ranging from continuous films and coatings to nano-objects. Because the size of the contact area with respect to the acoustic wavelength dictates the acoustic dispersion, we will describe separately continuous structures, in which the contact is large, before discussing micro- and nanostructured media, where the contact is localized.

Published under an exclusive license by AIP Publishing. <https://doi.org/10.1063/5.0220082>

09 August 2025 09:51:10

## TABLE OF CONTENTS

I. INTRODUCTION.....	0
II. LASER ULTRASONICS SETUPS: FROM MHZ TO GHZ.....	2
A. Generation .....	2
B. Detection schemes.....	3
III. BONDING AND DELAMINATION OF MM- TO $\mu\text{M}$ -THICK FILMS AND INTERFACIAL ADHESIVE LAYERS .....	4
A. Guided and interface waves.....	5
B. Evaluation of interfacial adhesives with Zero Group Velocities (ZGVs) .....	5
IV. NANOSCALE INTERFACES.....	6
A. Frequency-dependent reflection coefficient in 1D films.....	6
B. Adhesion and interlayer bonding of van der Waals materials .....	7
V. MICRO- AND NANO-OBJECTS.....	8
A. Single objects .....	8
B. Microsphere monolayers .....	9
C. 3D assemblies of micro- and nanoparticles .....	10
VI. CONCLUSION AND PERSPECTIVES .....	11

## I. INTRODUCTION

Interfaces are boundary regions between two distinct materials or states of matter, through which the exchange of various physical and chemical interactions can take place. In solids, an interface can be formed when two bodies come into contact, resulting in a mechanical interplay between them at one or several points. The governing mechanics of contact interfaces are multi-scale and can include macroscopic geometric features,<sup>1,2</sup> such as the presence of cracks, roughness, or porosities as well as microscopic adhesive interactions like van der Waals (vdW) forces.<sup>3,4</sup> In an ever-evolving landscape of materials engineering aimed at advancing device miniaturization and multi-functionality, understanding interfacial and contact mechanics has become pivotal. This understanding is particularly relevant for applications including the evaluation of interfacial adhesive bonding in composite structures,<sup>5,6</sup> micro/nanostructuration of thin films and coatings used in mechanical sensing and energy harvesting,<sup>7–10</sup> adhesion optimization of bio-functionalized surfaces and interfaces,<sup>11</sup> the assembly of 2D materials<sup>12</sup> as well as the design of metamaterials and crystals for phononic control and heat management.<sup>13</sup>

A large number of experimental techniques have been developed to assess bonding and interfacial mechanics. This includes peel tests,<sup>14</sup>

nanoindentation and nanoscratching,<sup>15</sup> and laser spallation techniques,<sup>16</sup> among many others. These approaches can yield large deformations and stresses and grant access to a wide range of interfacial bonding strengths and fracture toughnesses; however, they remain invasive in nature. Alternatively, nondestructive methods such as eddy-currents,<sup>17</sup> thermography,<sup>18</sup> or x-rays tomography<sup>19</sup> can give information about the structure and composition of contacting/joint interfaces but fail to quantify their mechanical properties. Acoustic-based methods are of great interest in this context, since, in addition to being nondestructive, they offer means to mechanically interrogate interface quality and adhesion, at various length and time scales. Pioneering works from Kendall and Tabor utilized the transmission and reflection of acoustic waves across interfaces.<sup>20</sup> They demonstrated that air gaps forming due to roughness blocked the transmission of acoustic waves, thereby reducing the effective contact area. Later, techniques using reflection and transmission of bulk acoustic waves at an imperfect interface<sup>21–24</sup> or propagation of guided waves in bonded structures<sup>25–28</sup> have been developed. Although less used, interface waves have also been proposed as interesting potentialities owing to their extreme sensitivity to the boundary conditions at the contacting interface.<sup>29–31</sup>

Acoustic waves can be generated classically using piezo-electric transducers in contact with the sample to emit and detect sound waves, with acoustic wavelengths typically up to a few hundreds of micrometers, offering sub-millimetric resolution. In these experiments, the frequency range is usually restricted to a few tens of MHz.<sup>32</sup> To overcome this limitation, scanning acoustic microscopy uses an acoustic lens to focus sound down to a diffraction-limited spot. At room temperature, the frequency range can be extended up to  $\sim 2$  GHz, using water as a coupling medium.<sup>33</sup> In cryogenic conditions, frequencies as high as 15 GHz have been reached in pressurized liquid Helium.<sup>34</sup> Such implementations require a coupling medium and cannot be performed *in situ*. In addition, the frequency range is narrow and does not allow probing acoustic dispersion over a large range of frequencies, which is characteristic of imperfectly bonded interfaces. Similarly, inter-digitated transducers, which allow generating and detecting surface waves (SAWs) and guided acoustic waves (GAWs) up to hundreds of MHz, are usually designed to operate at a single acoustic wavelength and do not give access to the full acoustic dispersion spectrum. In contrast, Laser Ultrasonics (LU) techniques are non-contact and allow the generation of broadband acoustic pulses with a frequency content extending up to a few THz, thanks to the thermoelastic expansion induced by the absorption of short laser pulses. In this review, we will explore the specificities of the generation/detection processes of the typical LU setups used to assess adhesion and nanocontact features from micro- to nanoscales.

To describe the dispersion of acoustic waves due to imperfect boundary conditions, lumped mechanical elements (i.e., springs, masses, and dashpots) are typically used. Interfaces having a large lateral extension with respect to the acoustic wavelength (i.e., those formed by thin solid films and coatings serving as adhesive/interfacial layers between two contacting materials) are classically modeled by a massless spring of stiffness per unit area  $K$  (in units of  $\text{Pa}\cdot\text{m}^{-1}$  or  $\text{N}/\text{m}^3$ ).<sup>22</sup> Such modeling leads to a discontinuity of the displacements  $\Delta u$  across the interface, while the stresses remain continuous and equal to  $K\Delta u$ . This model has been used to describe the acoustic propagation across thin interlayers,<sup>22,24,35</sup> rough interfaces,<sup>26,32,36</sup> or cracks.<sup>37,38</sup> On

the other hand, when considering micro- and nano-objects having interfaces of lateral extensions smaller than the acoustic wavelength (e.g., spheres, disks, or rods), it is convenient to describe the object as a linear surface oscillators of mass  $m$ , connected to the substrate via normal contact spring of linear stiffness  $k$  (in  $\text{N}/\text{m}$ ). In this situation, the contact is often mediated by adhesive forces, and  $k$ -values are predicted using contacts models such as Johnson-Kendall-Roberts (JKR) or Derjaguin-Muller-Toporov (DMT) models.<sup>39</sup> Given the different nature of the contact in these two situations, we will describe them separately in this review and consider first films, before discussing micro- and nano-objects.

Obviously, the size of the contacting structures will dictate the range of acoustic frequencies that must be employed to probe it. Similarly, the effective thickness of the interface will impact the behavior (propagation or resonance, depending on the size of the structures) of the acoustic waves interacting with it. At low frequencies (i.e., when the applied acoustic wavelength is much larger than the thickness of the interface), the spring constant  $K = C/l$  modeling the interface can alternatively be seen as a thin layer of thickness  $l$  and of rigidity  $C$ . The length  $l$  can either describe the thickness of a thin interfacial layer,<sup>24,35</sup> the width of a fracture,<sup>38,40</sup> or the average height of the asperities of a rough interface.<sup>26,32,36</sup> This description illustrates that the stiffness of the interface dictates the range of frequencies that are affected by the imperfect boundary. This is sketched in the interfacial stiffness spectrum shown in Fig. 1. In geophysics, for instance, due to the large scale of interfacial asperities, low spring constants (between  $10^8$  and  $10^{12}$   $\text{N}/\text{m}^3$ ) are considered at frequencies  $\leq 1$  kHz.<sup>38</sup> Higher spring constants (between  $10^{15}$  and  $10^{18}$   $\text{N}/\text{m}^3$ ) are considered in nondestructive testing of millimeter structures, where the acoustic frequencies can go up to hundreds of MHz,<sup>41</sup> while spring constants up to  $10^{19}$   $\text{N}/\text{m}^3$  can be found when probing nanometer-thick interfaces, such as those found in 0D, 1D, and 2D materials.<sup>42,43</sup>

LU gives access to a broad range of acoustic frequencies and, thus, offers the possibility to explore different contact regimes, with spring constant values spanning 8 decades. Below, we will first describe different LU schemes available that allow generating and probing frequencies from a few MHz to several tens of GHz. Then, we will review studies of mm- to  $\mu\text{m}$ -scale interfaces with sub-GHz techniques, mostly with guided and interface waves as well as zero group velocity modes. Moving to a higher frequency regime, we will discuss applications to nanoscale interfaces using picosecond ultrasonics (PU), largely based on bulk compressional waves and thickness mode resonances. All these interfaces are best described with interfacial springs from micro to nanoscales. We will finally present the contact of micro- and nano-objects that can be described by linear oscillators.

## II. LASER ULTRASONICS SETUPS: FROM MHZ TO GHZ

### A. Generation

In LU techniques, pulsed laser sources are used to generate various types of acoustic waves in the MHz-GHz range. Briefly, laser pulses are absorbed by an optically absorbing layer deposited on the surface of a sample of interest. Thin metallic films are typically well suited for this purpose. The optical absorption of the laser pulses induces a rapid thermoelastic expansion of the layer, which launches high frequency acoustic waves in the sample. For relatively long laser pulses, i.e., in the nanosecond range, the duration  $\tau_p$  of the laser pulse dictates the frequency content of the excited waves, with an upper limit that

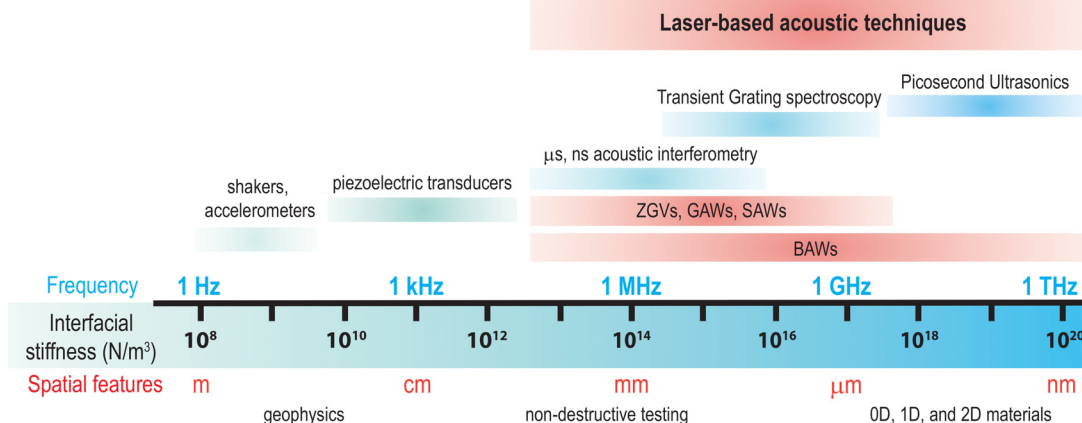


FIG. 1. The interfacial stiffness spectrum, in which opto-acoustic methods span from the MHz to the THz regime and can cover seven decades (from  $10^{13}$  to  $10^{20}$  N/m<sup>3</sup>).

can extend up to  $f = 1/\tau_p$  (typically 200 MHz for a 5 ns pulse emitted from Nd:YAG laser). Shorter pulses with  $\tau_p < 1$  ps can be used to generate hypersonic waves, a technique also called picosecond ultrasonics (PU).<sup>44</sup> In this regime, the frequency spectrum of the generated acoustic pulses is limited by the optical penetration depth in the metallic film,  $\xi$ . The peak of this frequency spectrum can be defined as<sup>45</sup>  $f_{PU} = V_L/2\pi\xi$ , where  $V_L$  is the sound speed of bulk longitudinal waves. For typical metals,  $V_L \sim 6000$  m/s and  $\xi \sim 10$  nm, which gives a frequency spectrum centered around  $f_{PU} \sim 100$  GHz. In some metals, the thermal diffusion will be fast enough to increase the effective in-depth extension of the thermoelastic source, thus decreasing the accessible frequency range.<sup>46</sup>

Because the generation mechanism relies on the thermoelastic expansion, the predominant bulk waves that are generated are the longitudinally polarized (L) waves. It is also possible to generate transversally polarized waves either by focusing the laser source<sup>47</sup> or using an anisotropic substrate cut off-axis<sup>48</sup> or also using metallic diffraction gratings.<sup>49</sup> When the pump beam is tightly focused on a surface, SAWs can also be generated in the lateral direction [see Fig. 2(a) for illustration], with a wavelength limited by the laser spot size. Typically, a spot size  $d = 2 \mu\text{m}$  can yield a SAW frequency spectrum extending up to  $\sim V_{SSL}/d = 3$  GHz, wherein  $V_{SSL}$  denotes the velocity of surface skimming longitudinal waves.<sup>50</sup> In addition, depending on the sample characteristic size compared to the acoustic wavelength (i.e., thick substrates acting as infinite and semi-infinite media; thin films acting as free-standing membranes; films adhering onto a thick substrate) and the spatial profile of the pump laser (i.e., grating patterns, or line and point source excitations), it is possible to generate different types of acoustic waves, including bulk acoustic waves (BAWs), SAWs, and guided acoustic waves (GAWs), as is illustrated in Fig. 2(a).

A largely used LU setup that relies on varying the spatial profile of the pump laser to generate sub-GHz SAWs and GAWs at a well-defined wavelength is called Transient Grating Spectroscopy (TGS).<sup>51</sup> In this setup, the pump beam is split into two excitation beams using the +1 and -1 diffraction orders of a phase mask. These diffracted beams are focused at the sample surface by a two-lens telescope system. The crossing of the pump beams forms a periodic interference pattern [see the grating excitation profile in Fig. 2(a) for illustration] with a periodicity imposed by the +1 and -1 diffraction angle. This

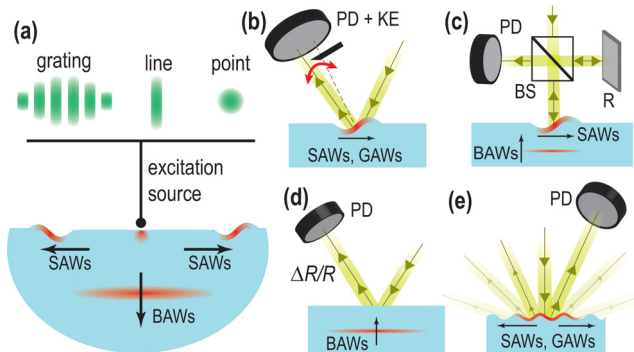


FIG. 2. (a) Schematic showing different spatial profiles (grating profile, line source, and point source) that can be applied to the excitation pulsed laser source in order to generate a variety of acoustic waves, including Bulk Acoustic Waves (BAWs), Surface Acoustic Waves (SAWs), and guided acoustic waves (GAWs). Optical detection schemes usually used in laser ultrasonics: (b) deflectometry, (c) interferometry, (d) reflectometry, and (e) diffractometry. PD: photodiode, KE: Knife-Edge, BS: Beam splitter, R: Reflector.

interference pattern generates SAWs at a fixed wavelength equal to the optical fringe spacing, ranging typically from  $2 \mu\text{m}$  to  $200 \mu\text{m}$ . To access acoustic frequencies up to 1 GHz, TGS' setups rely on picosecond laser pulses with  $\tau_p < 1$  ns for generation and avalanche photodiodes for detection.

## B. Detection schemes

Because the acoustic frequencies that are generated are so high, the detection of these laser-generated acoustic waves relies on the use of a second laser beam, the probe. Detection techniques can be broadly divided into four categories: deflectometry, interferometry, reflectometry, and diffractometry-based schemes. They are illustrated in Figs. 2(b)–2(e) and can be briefly described as follows. In deflection-based techniques [Fig. 2(b)], the probe light reflected off the surface is focused onto a photodiode while being partially blocked by a sharp object, usually a knife-edge<sup>52</sup> or an iris.<sup>53,54</sup> Changes in the surface slope caused by the propagation of SAWs deflect the probe, which

translates into a change in the intensity on the photodiode due to the partial masking of the probe light entering the photodiode. Movement of the surface can also alter the collimation of the reflected probe, and this distortion also allows probing acoustic waves.<sup>55</sup>

In contrast to deflectometry, which measures the change in surface slope and/or position, interferometric setups [Fig. 2(c)] allow measuring the normal displacement of the surface. They rely on the tracking of the reflection of a probe laser on the sample surface,<sup>56</sup> wherein the relative phase between a reference beam and beam reflected off the sample can be analyzed. Standard implementation can be based on Michelson, Sagnac,<sup>57</sup> common-path interferometers,<sup>58</sup> or other commercially available devices such as photorefractive two-wave mixing interferometers.<sup>59</sup> Alternatively, reflectometric techniques [Fig. 2(d)] measure changes in the refractive index inside the sample caused by the propagation of acoustic-induced compressions. In opaque samples, this effect offers the possibility to detect acoustic pulses due to the propagation of BAWs in the volume of bulk samples. In transparent samples, a grating of refractive index is formed with a spacing imposed by the acoustic wavelength. The photoelastic interaction of the probe light with the acoustic-induced optical grating produces the so-called Brillouin oscillations at a well-defined frequency. These techniques can be used in the time domain as in picosecond ultrasonics (PU)<sup>60</sup> or in spectroscopic schemes.<sup>61</sup>

Diffraction-based setups [Fig. 2(e)], notably TGS techniques, offer the possibility to measure the normal surface displacement caused by

the propagation of SAWs by tracking higher orders of diffraction of a diffracted probe light. In order to enhance the low amplitude diffracted signal, optical heterodyning is usually used by interfering a reference beam with the diffracted probe beam. For a more detailed explanation of the working principles, instrumentation, and practical consideration for the implementation of TGS setups, the reader can refer to reviews.<sup>51,62,63</sup> TGS gives access to the dispersion behavior (i.e., frequency-wavenumber diagrams) of SAWs and GAWs modes over a range of acoustic wavelengths spanning two orders of magnitude and typically ranging from 100 to 1  $\mu\text{m}$ .

### III. BONDING AND DELAMINATION OF mm- TO $\mu\text{m}$ -THICK FILMS AND INTERFACIAL ADHESIVE LAYERS

As we have discussed in the introduction, the nature of the contact differs greatly in films and in 3D objects. In this section, we will first review applications related to the probing of bonding and adhesion of half-spaces and thin films. The frequency of the acoustic waves also dictates the characteristic scale of interface that can be probed. We will first describe the MHz regime where the  $\mu\text{m}$ -scale corrugations of the contacting surfaces or the presence of a physical interfacial layer (third body) are the main actors in the degradation of the interface.

The classical description of the interface at that scale relies on linear spring constants per unit area,  $K$ , as is shown in Fig. 3(a). The vast majority of applications we describe use waves that propagate along

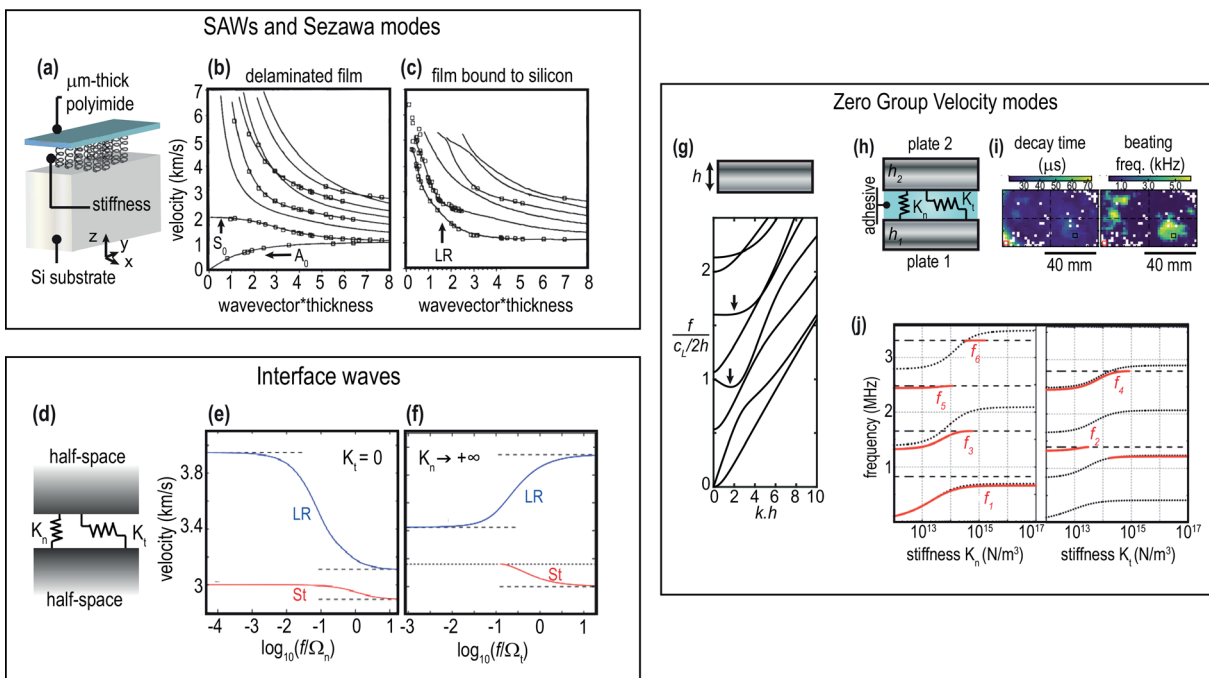


**FIG. 3.** (a) Schematic of the sample configuration studied using sub-GHz SAWs and GAWs in Ref. [64]. Dispersion curves of (b) a free-standing and (c) a tightly bound polyimide film measured with TGS. (d) Schematic of an imperfect interface between two half-spaces. Dispersion relations showing the behavior of Rayleigh and Stoneley waves for (e)  $K_n \rightarrow +\infty$  and (f)  $K_t = 0$ . (g) Dispersion curves of Lamb waves in a free-standing plate. (h) Schematic of the sample configuration studied using ZGVs in Ref. [65]. (i) Maps of decay time and beating of ZGVs in an adhesive tri-layered system.<sup>66</sup> (j) Variation of ZGV frequencies in a tri-layer system as a function of the normal and shear stiffnesses.<sup>65</sup> Panels (b) and (c) reproduced with permission from J. Adh. 50, 1 (1995). Copyright 1995 Taylor and Francis. Panels (e) and (f) reproduced from Valier-Brasier *et al.*, J. Appl. Phys. 112 (2012), with the permission of AIP Publishing. Panels (h) and (j) reproduced from Mezil *et al.*, Appl. Phys. Lett. 105 (2014), with the permission of AIP Publishing. Panel (i) reproduced from Hodé *et al.*, Appl. Phys. Lett. 116 (2020), with the permission of AIP Publishing.

the interface, i.e., SAW, GAW, or interface waves. Since such waves can have both normal and transverse motions, the interfaces are characterized by two spring constants per unit area  $K_n$  and  $K_t$ , which represent the resistance to motions parallel and perpendicular to the interface, respectively. For simplicity, the normal spring shown in Fig. 3(a) represents the resultant of both normal and transverse springs. Such modeling yields a discontinuity of the displacement fields and continuity of the stresses across the interface. When both spring constants are zero, the boundary conditions reduce to zero stress, which describes a completely delaminated case. In contrast, when both springs are infinitely stiff, the conditions reduce to stress and displacement continuity, which describes the tightly bound case. To illustrate these phenomena, we will review applications using different wave types.

### A. Guided and interface waves

Let us first describe the case of two solid half-spaces as is illustrated in Fig. 3(d). Based on the modeling described earlier, it is instructive to introduce normal ( $\Omega_n$ ) and transverse ( $\Omega_t$ ) characteristic frequencies defined as<sup>67</sup>

$$\Omega_{n,t} = \frac{K_{n,t}}{\rho V_{f,s}}, \quad (1)$$

where  $\rho$  is the density and  $V_f$  and  $V_s$  are the phase velocities of the fast (i.e., waves dependent on the normal spring component) and slow (i.e., waves dependent on the shear spring component) interface waves, respectively. In such case, it has been shown that, when  $K_t = 0$ , the dispersion curves of leaky SAWs [also referred to as Leaky Rayleigh (LR) waves] and interface waves propagating between the two solid half-spaces known as Stoneley (St) waves, can be described by two dispersion curves plotted in the non-dimensional space  $f/\Omega_n$ , as can be seen in Fig. 3(e). The transition between the slip and free interface behaviors is, thus, determined by  $\Omega_n$ . When  $K_n \rightarrow +\infty$ , the dispersion curves are obtained when plotting against the non-dimensional frequency  $f/\Omega_t$  as can be shown in Fig. 3(f). In this case,  $\Omega_t$  determines the transition between slip and welded interface behaviors. Furthermore, such analysis reveals a cutoff frequency,  $f_c$ , proportional to  $1/K_t$ , below which Stoneley waves do not exist. This observation shows that the quality of interface can not only introduce dispersive behaviors but can also control the existence of certain types of interfacial acoustic modes.

When the thickness of the contacting materials becomes comparable to the acoustic wavelength, guided waves can also be used. An early study by Rogers and Nelson reported on the use of TGS to assess the bonding quality of micrometer-thick polyimide films deposited on silicon substrates<sup>64</sup> [see Fig. 3(a) for sample configuration] by comparing the propagation of sub-GHz SAWs and GAWs in delaminated and fully bonded samples. While both samples had identical intrinsic mechanical properties (density and elastic moduli), their measured dispersion curves revealed drastic quantitative and qualitative changes. In particular, as is shown in Fig. 3(b), delaminated films showed a dispersive behavior similar to Lamb waves guided in a free-standing layer, where  $S_0$  and  $A_0$  modes are clearly identified [see arrows in Fig. 3(b)]. In contrast, when a thin layer is tightly bonded to a substrate [see Fig. 3(c)], its acoustic response can be described by that of a layer supported on a half-space, wherein dispersive acoustic modes known as Rayleigh-Lamb or Sezawa modes can be observed in the layer, with the

first mode (denoted by LR in 3c) starting at the Rayleigh speed in the substrate and tending to the Rayleigh speed in the layer at high wave-numbers. This observation highlights the profound impact of adhesion on the existence of guided modes in the film.

It is worth mentioning that, in the case of adhesive films, it is important to consider the position of the excitation source in order to interpret correctly the dispersion of the acoustic waves. More specifically, a recent study by Robin *et al.*<sup>68</sup> has shown that when the source is located at the free surface of the film, the measured dispersion curves tended to unsupported, free-standing Lamb wave dispersions when the film-substrate adhesion is decreased, as was the case in Fig. 3(b). This is due to the fact that the excited GAWs will be confined in the layer rather than being coupled to the substrate. In contrast, when the source is located at the film-substrate interface, one would measure a dispersion curve similar to that measured on a free substrate (i.e., a SAW dispersion rather than a Lamb wave dispersion) for a poor film-substrate adhesion, since in this case, the acoustic energy is confined in the substrate rather than the film. This study shows that the position of the laser pump beam influences the measured dispersion curves and has to be accounted for when dealing with imperfect adhesive films.

### B. Evaluation of interfacial adhesives with Zero Group Velocities (ZGVs)

There is also a significant body of literature that uses a special type of long-lived Lamb waves, known as Zero Group Velocity (ZGV) Lamb modes to assess adhesive bonding. These Lamb modes are polarized in the sagittal plane and occur when the group velocity vanishes for a finite value of wavenumber.<sup>69–71</sup> To illustrate this, we show in Fig. 3(g) the typical Lamb wave dispersion curves for a plate of thickness  $h$ , bulk wave velocities equal to  $C_L = 6000$  and  $C_T = 3200$  m/s, and density  $\rho = 2500$  kg/m<sup>3</sup>, wherein ZGV modes are indicated in arrows. Due to their locally resonant nature and long-lived oscillations, ZGVs are characterized by their high quality factors, which makes them highly sensitive to assess the bonding and adhesive quality.

Mezil *et al.* used laser-generated ZGVs to quantify the normal and tangential interfacial stiffnesses of tri-layer systems consisting of mm-thick glass plates bonded to each other by various adhesive layers<sup>65</sup> [see Fig. 3(h)]. They revealed that such multilayered plate assembly can support more ZGV modes than a single plate, and that their resonant frequencies and cutoffs significantly depend on the normal and shear interfacial stiffnesses, as can be seen in Fig. 3(j). To generate ZGVs in these samples, they used nanosecond pulsed lasers (typically  $\tau_p \sim 10$  ns pulse duration) and large spot sizes, with a beam diameter typically on the order of the thickness of the sample. Since the frequency of these excited modes is typically below 10 MHz in mm-thick plates, the detection can be accomplished by measuring the normal displacement of the sample surface using low-MHz interferometry-based setups.

The authors also compared liquid adhesive layers (water or oil) that exhibit small shear stiffness to solid ones (epoxy). In the case of two plates of thickness 1.5 mm bonded by a 35  $\mu$ m epoxy adhesive layer,<sup>59</sup> they showed that the first symmetric and anti-symmetric ZGVs can be sensitive to  $K_n$  and  $K_t$ , respectively. When bonded with a liquid layer, i.e., water and oil droplets, the frequencies of the identified ZGV peaks were found to be very similar to a single plate resonance frequencies, indicating the presence of a very weak shear stiffness  $K_t$ . The value of such weak shear stiffness could not be precisely

determined at the experimentally measured frequencies but was estimated to be  $<10^{11}$  N/m<sup>3</sup>. In contrast to liquid bonding layers, when the two plates were bonded with solid adhesives such as salol or epoxy, low-MHz ZGV measurements yielded interfacial stiffnesses on the order of  $10^{15}$  and  $10^{14}$  Pa/m for  $K_n$  and  $K_t$ , respectively.

In parallel to the possibility of exploiting the resonant frequency of ZGV modes, Hode *et al.* looked at the attenuation and wave mixing of these modes to probe adhesive bonding quality in tri-layered systems.<sup>66</sup> By degrading the adhesion between two aluminum plates via the introduction of cohesive and adhesive defects, the authors demonstrated the capacity to discriminate between strong and weak bonding. To do so, they mapped the ZGV resonance decay time and beating frequencies of two closely spaced resonances across the interface and localized adhesive defects in the tri-layer structures, as is shown in Fig. 3(i). These findings demonstrate the versatility of acoustics features that are accessible with LU-based ZGV measurements, in order to better understand bonding mechanics at the mesoscale.

#### IV. NANOSCALE INTERFACES

At the microscale, the quality of the interface depends mainly on the heterogeneous conformation of the contacting surfaces or the presence of an interfacial layer, as we have seen in Sec. III. At a smaller scale, adhesion can be mediated by surface chemistry, ion implantation, van der Waals forces, and nano-roughness. Such phenomena usually yield very stiff interfaces with  $K \gtrsim 10^{17}$  N/m<sup>3</sup> and require

high-frequency probing (typically  $\gtrsim 1$  GHz) to assess their bonding strengths. This is naturally the realm of picosecond ultrasonics where hypersonic waves can be generated thermo-elastically using femtosecond laser pulses<sup>44</sup> with  $\tau_p < 1$  ps. This technique has been implemented to either probe the reflection of longitudinal BAWs off contacting interfaces between sub-micron thin films and substrates or to investigate the vibrational spectra of sub-micron resonant thin films adhering to substrates.

#### A. Frequency-dependent reflection coefficient in 1D films

By probing longitudinal waves propagating through thin films and reflecting off a contacting interface [Fig. 4(a)], it is possible to measure the acoustic reflection coefficient  $r$ , whose response will be strongly dependent on the elastic interfacial coupling between the film and its substrate. Since the geometry can be approximated as 1D due to lateral dimensions of the laser source being much larger than the thickness of the sample, the typical model used to describe the contact-based behavior of  $r$  is that of two media connected by massless longitudinal spring of interfacial stiffness  $K_n$  as in Sec. III [see Fig. 4(a)]. In this context, the reflection coefficient between two media of indices  $i = 1, 2$  is

$$r = \left| \frac{Z_1 - Z_2 + i\omega Z_1 Z_2 / K_n}{Z_1 + Z_2 + i\omega Z_1 Z_2 / K_n} \right|, \quad (2)$$

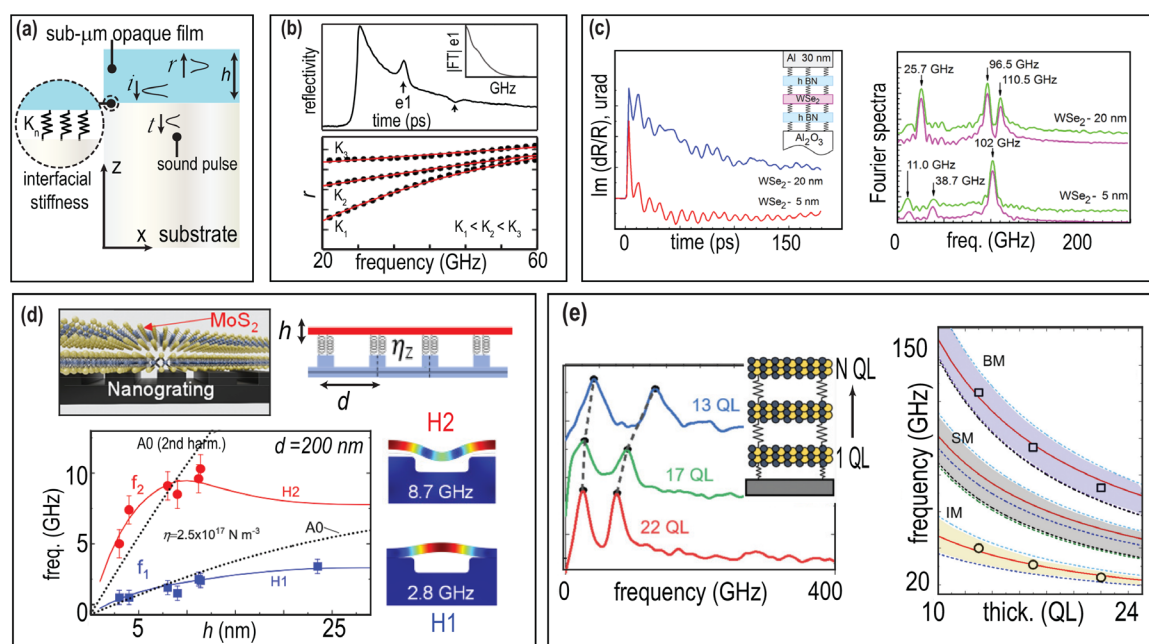


**FIG. 4.** (a) Schematic showing the propagation and reflection of a GHz acoustic pulse in a sub-micron opaque thin film adhering to a substrate. The film-substrate interface is modeled by a spring of interfacial stiffness  $K_n$ . (b) Typical time domain signal obtained in PU. The acoustic pulse propagating in the film is observed in the form of echoes (indicated by arrows) after each round trip. Variation of the acoustic reflection coefficient as a function of the frequency for three different  $K_n$  values as per Eq. (2). (c) Time domain and Fourier spectra of thickness mode resonances of nm-thick vdW multilayered materials adhering onto a sapphire substrate. (d) Variation of the thickness resonance of vdW material as a function of its thickness and its adhesion to a nanostructured surface. (e) Variation of the eigenvibration of vdW multilayers as a function of their thickness measured in number of quintuple layers QL. Panel (b) reproduced from Abi Ghanem *et al.*, *J. Biophoton.* 7, 453 (2014). Panel (c) reproduced with permission from *Nano Letters* 22, 2070 (2022). Copyright 2022 American Chemical Society. Panel (d) reproduced from Yan *et al.*, *Nano Lett.* 22, 6509 (2022), licensed under a Creative Commons Attribution (CC BY) license. Panel (e) reproduced with permission from Park *et al.*, *Nanoscale* 13, 19264 (2021). Copyright 2021 Royal Chemical Society.

where  $Z_i$  is the acoustic impedance and  $\omega$  is the angular frequency.

It is instructive here to define a characteristic frequency  $f_{ref}$  using this model.<sup>72–74</sup>

$$f_{ref} = \frac{K_n(Z_1 + Z_2)}{2\pi Z_1 Z_2}. \quad (3)$$

When  $f \ll f_{ref}$ , the interface can be treated as welded, and the reflection coefficient tends to  $r = (Z_1 - Z_2)/(Z_1 + Z_2)$ . In contrast, for  $f \gg f_{ref}$ ,  $r$  tends to one, indicating that at high frequencies, the film would effectively behave as a free-standing, unsupported membrane with total acoustic reflection. At intermediate frequencies, a dispersion in  $r$  can be observed.

When probing thick films (i.e.,  $h > 100$  nm) with PU, one can temporally resolve pulses of picosecond duration (usually tens of ps) that propagate back and forth in the film in the form of longitudinal echoes, due to reflections at the sample interfaces, as is shown in the upper panel of Fig. 4(b). By taking the amplitude ratio of two successive echoes, one can obtain the reflection coefficient  $r$ . When pressing together surfaces with nano-roughness, it has been shown that  $|r|$  is proportional to the contact pressure.<sup>43</sup> This observation has been partially explained by considering that each subwavelength contacting asperity acts as an acoustic scatterer. The random distribution of asperities along the interface, thus, acts as a discontinuous acoustic source, effectively reducing the reflected amplitude. This description, however, only partly captures the observed reduction in  $r$ , suggesting that the vibrational eigenmodes of the asperities themselves should play a role. In addition to the magnitude of the reflection coefficient, the arrival times of the acoustic pulses can also indicate plastic deformation of the contacting asperities.<sup>43</sup>

Each echo contains a broadband frequency content [inset of Fig. 4(b)] that extends tens of GHz. The frequency dependence of the reflection coefficient  $r(f)$  [see bottom panel in Fig. 4(b)] can be obtained via a Fourier transform of the pulses or via time-frequency diagrams using, for instance, a wavelet analysis.<sup>75</sup>  $r(f)$  can then be fitted using Eq. (2) with  $K_n$  as a free parameter. Such approach has been adopted to map the adhesion of single biological cells on titanium surfaces.<sup>75,76</sup> Note that to fully benefit from this approach, it is necessary to account for attenuation due to viscoelastic damping in the layer that can introduce an additional frequency dispersion.<sup>77</sup>

In contrast to thick films, when dealing with samples typically thinner than 100 nm, echoes cannot be resolved in time. Instead, the acoustic energy is quantized into thickness mode resonances, which radiate into the substrate via the film-substrate interface, causing damped oscillations. The acoustic reflection coefficient can be retrieved from the decay rate  $\Gamma$  of these oscillations,

$$r = \exp(-2h\Gamma/V_L), \quad (4)$$

where  $h$  is the thickness of the film and  $V_L$  is the longitudinal wave velocity in the resonating film. When several films with increasing thicknesses are probed, it is possible to obtain the  $K_n$  value of the interface by equating both Eqs. (2) and (4) and fitting the variation of  $\Gamma$  vs  $h$ . This approach has been used to probe the bonding of ultrathin metallic layers to substrates. This includes the bonding of gold nanofilms to silica<sup>72</sup> and silicon substrates. In the latter case, the effect of ion implantation<sup>42</sup> and the use of self-assembled molecular monolayers as intermediate bonding layer<sup>78</sup> were examined.  $K$ -values ranging between  $10^{18}$  and  $10^{19}$  N/m<sup>3</sup> have been measured in these studies

and were interpreted as a distribution of bonds described by a Lennard-Jones potential.<sup>42</sup> Similar values were later found for aluminum films adhering on silicon<sup>77</sup> and on sapphire.<sup>73</sup> Interfaces of variable bonding chemistry, obtained via self-assembled molecular monolayers sandwiched between a quartz substrate and a transfer-printed gold film, have also been evaluated using the decay rate of thickness resonances.<sup>79</sup>

## B. Adhesion and interlayer bonding of van der Waals materials

In recent years, along with probing the bonding strength of ultra-thin metals, the use of PU has been expanded to cover van der Waals (vdW) crystals and heterostructures. In this family of materials, strongly bonded 2D layers (in-plane, called “flakes”) are bound in the third dimension (out-of-plane) via weak interlayer (vdW) interactions. Such materials include transition metal dichalcogenides (e.g., MoSe<sub>2</sub>, WSe<sub>2</sub>, etc.), metal chalcogenides (e.g., InSe, GaSe, etc.), and hexagonal boron nitride (hBN). In an effort to better understand the weak mechanical coupling between the 2D layers in these materials, many works have lately begun to look at their GHz to THz resonant behavior by means of PU. Among those works, Klokov *et al.* studied the vibrational response of vdW heterostructures composed of hBN and WSe<sub>2</sub> flakes  $\leq 20$  nm in thickness, as is illustrated in Fig. 4(c).<sup>73</sup> They measured the time domain response and analyzed the corresponding Fourier spectra that contain several peaks due to the resonant behavior of this chain-like material. To interpret these data, they developed a multilayered mechanical chain model that incorporates substrate-layer normal stiffness and interlayer stiffnesses that describe vdW bonds. From their model, they deduced  $K$ -values for weak vdW interactions that are on the  $10^{18}$  N/m<sup>3</sup> order. Using a similar chain model analysis, Park *et al.* measured the interlayer vibrations of layered Bi<sub>2</sub>Se<sub>3</sub> vdW thin films [Fig. 4(e)].<sup>80</sup> By varying the thickness of these films, the authors provided an accurate model to estimate and precisely control the vibrational spectrum of these nanofilms.

In parallel to multilayers, there exist other types of vdW structures that have been explored with PU, wherein the interlayer and substrate-layer coupling played a key role in the outcome of the structure's vibrational spectrum. For instance, a recent work by Li *et al.* measured the breathing mode of freely suspended, nm-thick, MoSe<sub>2</sub>/WSe<sub>2</sub> bilayers as a function of the stacking angle.<sup>81</sup> Using the measured resonant frequency of this mode, which was found to be independent of the stacking angle, the authors deduced the stiffness of the vdW elastic bond between MoSe<sub>2</sub> and WSe<sub>2</sub> monolayers to be  $K_{vdW} \sim 6 \cdot 10^{19}$  N/m<sup>3</sup>. Wang *et al.* reported  $K$ -values on the same order between bi-layer and tri-layer MoS<sub>2</sub> on flat sapphire substrates using THz vibrational modes.<sup>82</sup> In contrast, a recent study by Yan *et al.* showed that nanostructuration of the supporting substrate can significantly decrease the substrate/MoS<sub>2</sub> contact stiffness, with  $K$ -values reaching  $10^{17}$  N/m<sup>3</sup>.<sup>83</sup> In this study, the authors also explored the possibility to tailor the phononic response of MoS<sub>2</sub> flakes by controlling their elastic coupling with the substrate [Fig. 4(d)], opening the possibility to systematically tune that coupling to design novel GHz and THz phononic devices.

Delamination of vdW materials can also be revealed by looking at a transition in their thickness resonance spectrum. As the interface bonding is degraded,<sup>84,85</sup> a transition from a fixed-free (perfect

interface) thickness resonance, whose frequency takes the form of a quarter-wavelength resonator

$$f_{QW} = (2n - 1)V_L/4d, \quad (5)$$

to a free-free (broken interface) one, whose form follows a half-wavelength resonator

$$f_{HW} = nV_L/2d, \quad (6)$$

where  $n = 1, 2, \dots$  indicates the mode number can occur. As stated by Antonelli *et al.*, this is analogous to clinking wall tiles to know whether they are well glued or not.<sup>72</sup> This approach has been notably used to investigate the substrate elastic coupling of several vdW materials<sup>86</sup> as well as complex oxides.<sup>85</sup> Furthermore, Greener *et al.* exploited this feature to scan spatially the elastic coupling between vdW nanolayers and sapphire substrates.<sup>84</sup> By producing 2D spectral density images at different resonant frequencies and assigning quarter and half-wavelength resonances to their probed regions, they demonstrated the ability to image both perfect and broken interfaces as well as interfaces of mixed nature, wherein both cases can be present within the probing spot.

## V. MICRO- AND NANO-OBJECTS

### A. Single objects

To transition from films to single objects, it is instructive to first review the situation when the contact area becomes comparable to the acoustic wavelength. For example, Dehoux *et al.* studied the transmission of acoustic pulses through the contact of single core/shell micro-capsules placed on a Ti substrate.<sup>87</sup> For such small capsules (typically of 5  $\mu\text{m}$  radii), the authors estimated a contact area of radius  $R_c = 0.3 \mu\text{m}$  using the Johnson-Kendall-Roberts (JKR) theory.<sup>88</sup> Owing to Ti-shell contact, a coherent phonon pulse is transmitted to the capsule, propagating through the shell and into the core as is shown in the schematic of Fig. 5(a). The photoelastic interaction of the probe light with the acoustic pulse propagating in the transparent capsule produced Brillouin oscillations at a well-defined frequency,  $f_c$ , as is shown in the optical reflectivity plot of Fig. 5(a). Via Brillouin oscillations, the

authors studied the phonon lifetime in the core of the capsule. They observed a non-exponential decrease in the lifetime that could not be explained by 1D wave theories. Considering  $R_c$  as the width of a piston-like acoustic source acting at the metal-sphere interface, they calculated the near-field limit  $z_{NF}$ ,

$$z_{NF} = R_c^2 f_c / v_c, \quad (7)$$

where  $f_c$  and  $v_c$  denote the acoustic frequency and sound velocity in the core of the capsule, respectively. Beyond  $z_{NF}$ , phonons may transit from the near to the far field of the acoustic source within the probed area of the core, which explains the non-exponential attenuation profile observed inside the capsule. This feature shows that, when the contact area becomes comparable to the acoustic wavelength, it can act as a local acoustic source that creates unusual transmission patterns that occur and can offer information about the contact as well.<sup>89</sup>

Within a similar context of contact-based acoustic emission, but at a smaller scale, 400  $\times$  120 nm diameter copper nanowires were dropped on a 10  $\mu\text{m}$  Si membrane.<sup>90</sup> Using the PU technique, the authors triggered acoustic vibration of these single nanowires and mapped, in space and time, the transmission of their resonant frequencies through the Si membrane as is shown in Fig. 5(b). Figure 5(b) (bottom) shows a 2D map of the acoustic emission of the copper nanowire in the bulk, and Fig. 5(b) (top right) shows two signals taken along (blue line) and across (orange line) the nanowire, respectively. They reveal a clear anisotropy in the acoustic emission of the nanowire due to the high aspect ratio of the contact area between the nanowires and the substrate, which acts as the acoustic source. Such acoustic radiation/transmission, which is the result of the radial breathing mode leaking through the nanorod-substrate contact channel, could be further leveraged to estimate the contact area between nanowires and substrates.

In addition to acoustic emission/radiation enabled via the contact features of single objects, one can also probe the vibrational spectrum of such objects that are smaller than, or on the order of, the acoustic wavelength by looking at their resonant modes. These modes will depend on the mechanical properties and shape of the objects and can include fundamental and harmonic modes. As discussed with

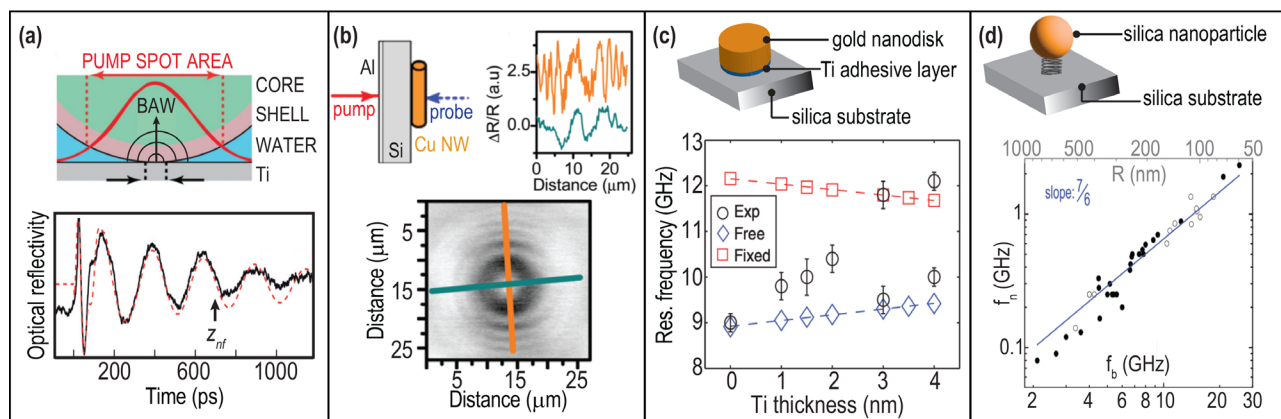


**FIG. 5.** (a) Time domain Brillouin oscillations in single core/shell microcapsules. (b) Acoustic radiation of a vibrating copper nanowire deposited on silicon. (c) Variation of the breathing mode of gold nanodisks as a function of the thickness of a Ti used as an adhesive layer. (d) Plot showing the scaling law between axial contact resonance and breathing modes of single gold nanoparticles adhering to glass substrate. Panel (a) reproduced from Dehoux *et al.*, Soft Matter 8, 2586 (2012). Panel (b) reproduced with permission from Jean *et al.*, Nano Letters 16, 6592 (2016). Copyright 2016 American Chemical Society. Panel (c) reproduced from Chang *et al.*, Nat. Comm. 6, 7022 (2015). Copyright Springer Nature 2015. Panel (d) reproduced with permission from Guillet *et al.*, Phys. Rev. B 86, 035456 (2012). Copyright 2012 American Physical Society.

thickness resonances of thin films, the frequency of the resonant modes of an object largely depend on the boundary conditions of the substrate on which they are deposited. The PU technique has been used to measure the breathing mode of single gold nanodisks adhering on a glass substrate via titanium layers of varied thicknesses used as an adhesive layer<sup>91</sup> as is shown in Fig. 5(c). It was found that the frequency of the breathing mode increases with increased Ti thicknesses due to contact stiffening between the gold and the glass substrate. More specifically, one can access a full range of adhesion coupling, spanning from non-binding to perfect adhesion by simply increasing the Ti layer thickness from none to 3 nm, suggesting that this adhesion control capability could be leveraged to tune the acoustic phonon frequency of a nanostructure between two extreme cases (i.e., a free-standing nano-object vs a nano-object perfectly attached to its substrate) in the GHz range.

In conjunction with the intrinsic mechanical resonances of nano-objects (for instance, the breathing modes), other contact-based resonant modes specific to the coupling between the object and the substrate can also be harnessed. In this context, Guillet *et al.* studied the GHz vibrational dynamics of single nanospheres with variable radii  $R$  ranging between 50 and 1000 nm, adhering to a flat substrate<sup>92</sup> [see Fig. 5(d)]. In addition to the excitation of the nanoparticles' breathing modes  $f_b$  (i.e., the spheroidal resonances) at frequencies above 1 GHz, the authors observed vibrational modes characterized by lower resonant frequencies,  $f_n$ , typically below 1 GHz. To interpret their observation, they represented the nanoparticles as linear surface oscillators of mass  $m$ , connected to the substrate via normal contact spring of stiffness  $k_n$ . The resonant frequency of such mass-spring oscillator is

$$f_n = \frac{1}{2\pi} \sqrt{\frac{k_n}{m}}, \quad (8)$$

where  $k_n$  represents a linear stiffness in N/m, in contrast to the interfacial stiffness per unit area  $K_n$  (in N/m<sup>3</sup>) that was discussed in Secs. III and IV. Using classical contact models that describe the contact between an elastic sphere and a flat substrate under the presence of adhesive forces, such as JKR or Derjaguin-Muller-Toporov (DMT)<sup>39</sup> models, and linearizing the force-displacement curves around the static equilibrium point, one can find that

$$k_n \propto R^{2/3}. \quad (9)$$

Since the nanoparticle mass  $m \propto R^3$  and the nanosphere's intrinsic breathing resonance are inversely proportional to its radius  $f_b \propto R^{-1}$ ,<sup>93</sup> one can relate the axial contact resonance  $f_n$  and the breathing resonance  $f_b$  via a power-law dependence, such that

$$f_n \propto f_b^{7/6}. \quad (10)$$

By simultaneously measuring  $f_b$  and  $f_n$ , Guillet *et al.* were able to confirm this simple scalability relationship derived from classical adhesion theories.

We have previously discussed how the intrinsic resonant modes of nanostructures can greatly be altered by the boundary conditions of the substrate on which they are deposited. Similarly, the contact between microspheres can also affect their spheroidal resonance spectrum. To scrutinize this effect, Dehoux *et al.* used the PU technique to generate and detect whispering gallery modes, also known as Rayleigh modes, in a dumbbell composed of two contacting glass microspheres

deposited on a soft substrate.<sup>94</sup> When the two microspheres are contacting along the equatorial perimeter, the contact between them is subject to an oscillating stress that couples their resonances. In this situation, specific modes have been observed to be greatly enhanced. This observation suggests that quality and the number of contacts between spheres, both in a 2D and a 3D geometry, will select resonant modes according to their symmetry in motion, leading to a selection of resulting collective motions of microsphere monolayers.

## B. Microsphere monolayers

2D micro- and nanospheres monolayers can be formed using various colloidal self-assembly schemes by leveraging direct assembly methods or liquid interface-mediated techniques.<sup>95</sup> The collective dynamics of such monolayers involving sphere-to-sphere and substrate-sphere contacts has also been shown to interact with the propagation of SAWs and GAWs in the sub-GHz regime. More specifically, it has been shown that Rayleigh waves propagating in semi-infinite substrates,<sup>96</sup> or flexural Lamb modes traveling in micrometer- and sub-micron-thick free-standing membranes,<sup>97,98</sup> can couple to local contact resonances of the microspheres deposited on top, as is shown in Fig. 6(a). This coupling causes the Rayleigh mode- or the flexural guided mode- to split into two branches: a lower branch that asymptotically approaches the microsphere resonant frequency and an upper branch that tends to the Rayleigh wave speed in the substrate (or the  $A_0$  wave speed in the membrane). As such, attenuation zones in select frequency ranges, also referred to as phononic bandgaps, can be observed in the dispersion behaviors of the propagating SAWs or GAWs. To describe this dispersive behavior, the microspheres can be modeled as an array of surface oscillators interacting with the substrate via axial contact springs of stiffness  $k_n$  [see inset of Fig. 6(a)] as described in Sec. V A for a single sphere.<sup>92</sup>

When the contacts between the spheres themselves become effectively more "stiff," the monolayer can sustain more vibrational modes, in addition to the sole axial mode discussed earlier, due to collective motion of the spheres, including rotational and shear modes. In this situation, more modes can appear in the dispersion curves. By measuring laser-generated SAW pulses in a microsphere monolayer composed of 2 μm diameter silica microspheres deposited on a glass substrate,<sup>52</sup> Hiraiwa *et al.* observed the presence of three resonant attenuation zones, a signature of three collective contact-based vibrational modes [see Fig. 6(b)]. To interpret their observation, they used a contact model<sup>99</sup> involving sphere-to-sphere contacts, in addition to sphere-substrate contacts. More specifically, in this model, the microspheres were considered as rigid bodies, and the sphere-substrate and sphere-sphere contacts were represented as normal and shear springs, respectively, as is illustrated in the inset of Fig. 6(b). This model described displacements and rotations of the microspheres as well as sphere-to-sphere and sphere-substrate interactions. In addition to the purely axial mode  $f_n$  [see Eq. (8)] observed by Boehler *et al.*<sup>96</sup>, this model predicted two additional contact resonances of mixed horizontal-rotational character, with frequencies given by

$$f_{hr} = \frac{1}{2\pi} \left[ \left( \frac{k_s}{4m} \right) (20\gamma + 7 + \sqrt{400\gamma^2 + 120\gamma + 49}) \right]^{1/2}, \quad (11)$$

$$f_{rh} = \frac{1}{2\pi} \left[ \left( \frac{k_s}{4m} \right) (20\gamma + 7 - \sqrt{400\gamma^2 + 120\gamma + 49}) \right]^{1/2}, \quad (12)$$

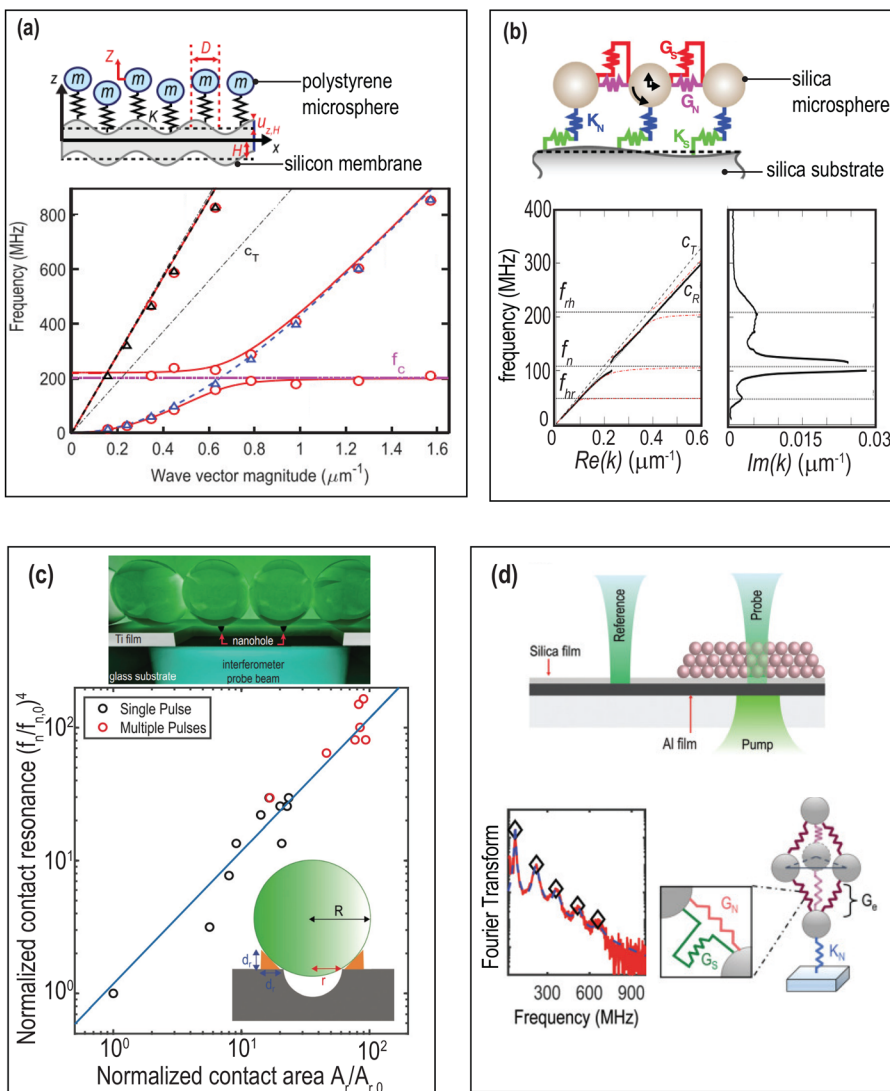


**FIG. 6.** (a) Lamb waves dispersion curves in a polystyrene microsphere monolayer adhered to a micrometer-thick free-standing silicon membrane. (b) SAW dispersion curves of a silica microsphere monolayer adhering onto a silica half-space. (c) Variation of the axial contact resonance of silica microspheres as a function of their contact area. (d) Longitudinal eigenvibrations of multilayer colloidal crystals. The plot shows a Fourier spectrum of a 12-layer-thick crystal. The schematics show the LU setup and the interfacial springs used in the modeling. Panel (a) reproduced from Khanolkar *et al.*, Appl. Phys. Lett. 107 (2015). Schematic figure in (b) reproduced from Hiraiwa *et al.*, Phys. Rev. Lett. 116, 198001 (2016) and the dispersion curves from Geslain *et al.*, J. Appl. Phys. 120 (2016). Panel (c) reproduced from Abi Ghanem *et al.*, Adv. Funct. Mater. 30, 1909217 (2020). Panel (d) reproduced from Abi Ghanem *et al.*, Nanoscale 11, 5655 (2019).

with  $\gamma = g_s/k_s$ , where  $k_s$  is the particle-substrate shear stiffness and  $g_s$  is the inter-particle shear stiffness. The authors showed the ability to tune the inter-particle spring stiffnesses by depositing an ultrathin metallic layer on top of the monolayer, thus shifting the frequency of the horizontal-rotational resonances  $f_{hr}$  and  $f_{rh}$  while leaving the vertical resonance  $f_n$  dictated by the substrate-particle normal stiffness unaffected. The presence of such resonant modes has then inspired the design of a new class of ultrasonic metamaterials for SAWs and GAWs, with contact-based sub-GHz phononic bandgaps.<sup>97,98,100–102</sup>

In a later study, Abi Ghanem *et al.* exploited the optical micro-lensing effect of silica microspheres to tune their normal contact resonance  $f_n$ . Briefly, when a laser is incident through the transparent spheres, it is focused on the opposite side due to the curvature of the sphere surface. This increases the fluence of the laser at the sphere/substrate interface, causing melting or ablation of the substrate.<sup>103</sup> This process changes the contact geometry between each sphere and the flat

substrate by modifying the contact from a point (i.e., Hertzian contact) to a ring-like geometry. As a result, the contact area increases, effectively increasing the contact stiffness and, therefore, inducing an upshift in the contact resonance. This phenomenon can be modeled using the Oliver-Pharr (OP) contact model, which describes the link between contact stiffness  $k_n$  and contact area  $A_c$  during elastic contact between an axisymmetric punch and an elastic half-space.<sup>104</sup> From this model, one can find that  $k_n \propto A_c^{1/2}$ . To calculate the contact resonance frequency, the punch can be considered to be a ring of contact area  $A_r = \pi(2rd_r + d_r^2)$  [see inset of Fig. 5(c)], where  $d_r$  is the width and  $r$  is the inner radius of the ring, leading to a simple 1/4 power-law between the normal resonant frequency and the ring contact area,

$$f_n \propto A_r^{1/4}. \quad (13)$$

Such modeling captures the link between the measured frequency and the contact area, as is shown in Fig. 6(c).

### C. 3D assemblies of micro- and nanoparticles

The contact-based dynamics of microspheres has also been extended to 3D, wherein crystals consisting of 390 nm diameter polystyrene spheres arranged into close-packed, ordered lattices with a thickness ranging from one monolayer, as described earlier, to twelve-layers thick<sup>105</sup> have been studied. Using laser-generated acoustic waves, the longitudinal eigen vibrations (i.e., organ-pipe modes) were measured in these systems. To describe the system, the spheres were considered as rigid bodies connected by massless springs; the particle-substrate contact was represented with a normal spring of stiffness  $k_n$ , and the particle-particle normal and shear contacts by axial and transverse springs of stiffnesses  $g_n$  and  $g_s$ , respectively, as is illustrated in Fig. 6(d). An effective contact stiffness  $g_e$  oriented along the out-of-plane direction was defined, which incorporates the contributions from the three pairs of inter-particle normal and shear contact springs. In these systems, fitting the measured vibration spectrum to the prediction of the model allowed extracting substrate-particle  $k_n$  and inter-particle  $g_e$  stiffnesses. However, comparing these values to those estimated using the DMT model sometimes exhibits a large discrepancy, due, in part, to the formation of nanometric-sized bridges around the contacts, which can drastically affect the contact stiffnesses of the colloidal crystals. The presence of such nano-bridges strongly depends on the self-assembly process used to fabricate the samples. The presence of residue/impurities during self-assembly fabrication processes can also lead to the formation of well-like features around the substrate-particle contact,<sup>106</sup> which stiffens the normal spring stiffness  $k_n$  by effectively increasing the contact area.

Increasing the number of stacking in a 3D assembly can be accompanied by an increased disorder that can strongly affect the mechanical behavior of the structure. To elucidate that, Ayouch *et al.* studied the elasticity of disordered colloidal structures in 3D assemblies consisting of 10-nm diameter interconnected silica nanoparticles connected via van der Walls interactions or covalent bonds.<sup>107</sup> The colloidal films were 200-nm thick and were supported by a Si substrate covered by a 100 nm thick Pt layer (for phototransduction, see Sec. II). Using the PU technique, the authors measured quarter-wavelength resonances of these fixed-free films and extracted the effective longitudinal sound speed  $v_f$ . Using existing theories for the elasticity of granular media,  $v_f$  can be expressed as a function of an effective stiffness  $k_e$  describing the inter-particle contacts such that

$$v_f = D \sqrt{\frac{z k_e}{10 m}} \quad (14)$$

Here,  $D$  is the diameter of the particles,  $z$  is the average number of contacts per particle,  $m$  is the mass of the particle, and  $k_e = k_n + (2/3)k_s$ , with  $k_n$  being the normal stiffness and  $k_s$  the shear stiffness of the individual contacts. This analysis revealed that the contact stiffnesses of covalent-bonded layers almost double the ones obtained from the van der Walls bonds. It was later demonstrated that hardening of such structures could allow transitioning from weak van der Waals coupling to strong covalent-bond coupling.<sup>108</sup> These findings further the understanding of contact mechanics in colloidal crystals and provide new ways to tailor their dynamics, for instance using a rational control of contact stiffness via systematic deposition of solid bridges or short-chain polymers between the particles.<sup>109,110</sup>

### VI. CONCLUSION AND PERSPECTIVES

Throughout the examples we have given in this review, it becomes apparent that, in films, the frequency at which acoustic propagation is affected by the contact is intimately linked to the magnitude of the interfacial stiffness  $K$ . This is also reflected in Eq. (3) that shows that the higher the interfacial stiffness  $K$ , the higher the probing frequency needs to be. Broadly, since the interfacial stiffness can be viewed as an interfacial layer of thickness  $l$ , stiff micrometric layers, such as epoxy, lead to dispersion in the MHz range, while the liquid layer appears as not bonded.<sup>59</sup> In this regime, the use of low-MHz ZGVs waves generated with nanosecond pulses is best suited. At the other end of the spectrum, interfaces mediated by nano-roughness or vdW coupling affect wave propagation in the GHz range: this is the realm of picosecond ultrasonics where acoustic waves are generated by femtosecond laser pulses. In-between these two regimes, transient grating techniques fill the gap.

Similarly, if one wants to benefit from the resonant features of the contacting structures, the frequency range will be dictated by the size of the vibrating objects. In submillimeter to micrometric films or spheres, guided waves and resonant modes can be observed in the MHz range, calling for the use of laser ultrasonics or TG techniques. In nanostructures (films, spheres, or rods), PU is best suited. Taken together with the consideration that the stiffness of the interface also influences the frequency range would suggest that acoustic studies would only be relevant when the characteristic dimensions of the contact match the dimensions of the vibrating structure. The fact that dispersive behaviors can be observed at all scales suggests on the contrary that in some systems, there exist a continuum of—or at least several—adhesive regimes that might have different origins. In this light, it would be interesting to probe these cases with all the techniques we reviewed to obtain a complete description of the adhesion across different scales. Along those lines, it would also be tempting to study different types of acoustic waves across these scales. This could be done by changing the geometry of the sample in order to probe ZGVs at the GHz for instance,<sup>111</sup> or by shaping the excitation source using spatial light modulators, in order to finely excite specific regions and polarizations in the acoustic dispersion curves. Another possibility would be to leverage nonlinear frequency-mixing laser ultrasonics approaches to assess specific contact and interface parameters with enhanced sensitivity.<sup>112</sup> Pushing the frequency limit further, the use of semiconductor superlattices<sup>113</sup> allows reaching THz frequencies. Another approach, which consists of using extreme UV laser light with few femtosecond pulse durations in a TGS configuration, has demonstrated the generation of acoustic waves with wavelengths as small as 10 nm.<sup>114</sup> Alternatively, one could opt for hybrid solutions by combining AFM's lateral resolution with PU's axial one.<sup>115</sup> Such technologies would allow probing adhesive processes in an unexplored frequency range and at higher interfacial stiffnesses.

Another specificity of the absorption of laser by metals in PU is the excitation of free electrons that can also diffuse across the contact. In the case of non-conforming contacts, this effect can be harnessed to probe the real contact area since electrons cannot cross air gaps, in contrast to acoustic waves.<sup>116</sup> In both PU and lower frequency LU techniques that we have reviewed, the reflection coefficient of longitudinal waves propagating perpendicular to the contacting interface is analyzed. One can also use the so-called Plane Wave Synthesis (PWS),<sup>117</sup> in which longitudinal (L) and transverse (T) plane waves

propagating at any angle are generated numerically, in post-processing, from experimentally generated and detected cylindrical waves.<sup>118,119</sup> Such an approach provides a more complete characterization of the contact, and it would be interesting to extend it to the higher frequency regimes. Finally, recent advances in opto-acoustic technologies have enabled the design and commercialization of different LU setups,<sup>120</sup> including PU-based microscopes operating at tens of GHz, in addition to other low-cost options at lower frequencies.<sup>121</sup> These developments and readily available setups should alleviate the hurdles encountered with building opto-acoustic setups and should render their use more accessible and more appealing to different communities seeking to evaluate the adhesion and quality of nano-interfaces for various applications.

## AUTHOR DECLARATIONS

### Conflict of Interest

The authors have no conflicts to disclose.

### Author Contributions

**Maroun Abi Ghanem:** Writing—original draft (equal); Writing—review and editing (equal). **Thomas Dehoux:** Writing—review and editing (equal).

### DATA AVAILABILITY

Data sharing is not applicable to this article as no new data were created or analyzed in this study.

### REFERENCES

- <sup>1</sup>K. L. Johnson and K. L. Johnson, *Contact Mechanics* (Cambridge university Press, 1987).
- <sup>2</sup>A. C. Fischer-Cripps, *Introduction to Contact Mechanics* (Springer, 2007), Vol. 101.
- <sup>3</sup>W. W. Gerberich and M. Cordill, *Rep. Prog. Phys.* **69**, 2157 (2006).
- <sup>4</sup>J. N. Israelachvili, *Intermolecular and Surface Forces* (Academic Press, 2011).
- <sup>5</sup>M. D. Banea and L. F. da Silva, *Proc. Inst. Mech. Eng., Part L: J. Mater.: Des. Appl.* **223**, 1 (2009).
- <sup>6</sup>S. Budhe, M. Banea, S. De Barros, and L. Da Silva, *Int. J. Adhes. Adhes.* **72**, 30 (2017).
- <sup>7</sup>S. R. A. Ruth, V. R. Feig, H. Tran, and Z. Bao, *Adv. Funct. Mater.* **30**, 2003491 (2020).
- <sup>8</sup>X. Liu, W. Liu, Z. Ren, Y. Ma, B. Dong, G. Zhou, and C. Lee, *Int. J. Optomechatronics* **15**, 120 (2021).
- <sup>9</sup>X. Li, W. Sun, W. Fu, H. Lv, X. Zu, Y. Guo, D. Gibson, and Y.-Q. Fu, *J. Mater. Chem. A* **11**, 9216–9238 (2023a).
- <sup>10</sup>C. Wu, A. C. Wang, W. Ding, H. Guo, and Z. L. Wang, *Adv. Energy Mater.* **9**, 1802906 (2019).
- <sup>11</sup>M. Zhanianmanesh, A. Gilmour, M. M. Bilek, and B. Akhavan, *Appl. Phys. Rev.* **10**, 021301 (2023).
- <sup>12</sup>Z. Dai, N. Lu, K. M. Liechti, and R. Huang, *Curr. Opin. Solid State Mater. Sci.* **24**, 100837 (2020).
- <sup>13</sup>T. Vasileiadis, J. Varghese, V. Babacic, J. Gomis-Bresco, D. Navarro Urrios, and B. Graczykowski, *J. Appl. Phys.* **129**, 160901 (2021).
- <sup>14</sup>M. D. Bartlett, S. W. Case, A. J. Kinloch, and D. A. Dillard, *Prog. Mater. Sci.* **137**, 101086 (2023).
- <sup>15</sup>X. Wang, P. Xu, R. Han, J. Ren, L. Li, N. Han, F. Xing, and J. Zhu, *Nanotechnol. Rev.* **8**, 628 (2019).
- <sup>16</sup>H. Ehsani, J. D. Boyd, J. Wang, and M. E. Grady, *Appl. Mech. Rev.* **73**, 030802 (2021).
- <sup>17</sup>I. Kryukov and S. Böhm, *J. Adhes.* **95**, 874 (2019).
- <sup>18</sup>J. Schroeder, T. Ahmed, B. Chaudhry, and S. Shepard, *Compos. Part A: Appl. Sci. Manuf.* **33**, 1511 (2002).
- <sup>19</sup>S. Zheng, J. Vanderstelt, J. McDermid, and J. Kish, *NDT E Int.* **91**, 32 (2017).
- <sup>20</sup>K. Kendall and D. Tabor, *Proc. R. Soc. London Ser. A* **323**, 321 (1971).
- <sup>21</sup>H. Tattersall, *J. Phys. D: Appl. Phys.* **6**, 819 (1973).
- <sup>22</sup>M. Schoenberg, *J. Acoust. Soc. Am.* **68**, 1516 (1980).
- <sup>23</sup>A. Pilarski and J. L. Rose, *J. Appl. Phys.* **63**, 300 (1988).
- <sup>24</sup>S. Rokhlin and Y. Wang, *J. Acoust. Soc. Am.* **89**, 503 (1991).
- <sup>25</sup>V. Vlasie and M. Rousseau, *Wave Motion* **37**, 333 (2003).
- <sup>26</sup>V. Vlasie, S. de Barros, M. Rousseau, L. Champaney, H. Duflo, and B. Morvan, *Eur. J. Mech.-A/Solids* **25**, 464 (2006).
- <sup>27</sup>B. Le Crom and M. Castaings, *J. Acoust. Soc. Am.* **127**, 2220 (2010).
- <sup>28</sup>M. Castaings, *Ultrasonics* **54**, 1760 (2014).
- <sup>29</sup>G. S. Murty, *J. Acoust. Soc. Am.* **58**, 1094 (1975).
- <sup>30</sup>T. Hsieh, E. Lindgren, and M. Rosen, *Ultrasonics* **29**, 38 (1991).
- <sup>31</sup>L. J. Pyrak-Nolte, J. Xu, and G. M. Haley, *Phys. Rev. Lett.* **68**, 3650 (1992).
- <sup>32</sup>B. Drinkwater, R. Dwyer-Joyce, and P. Cawley, *Proc. R. Soc. London Ser. A* **452**, 2613 (1996).
- <sup>33</sup>Z. Yu and S. Boseck, *Rev. Mod. Phys.* **67**, 863 (1995).
- <sup>34</sup>M. Muha, A. Moulthrop, G. Kozlowski, and B. Hadimoglu, *Appl. Phys. Lett.* **56**, 1019 (1990).
- <sup>35</sup>S. Rokhlin and Y. Wang, *J. Acoust. Soc. Am.* **91**, 1875 (1992).
- <sup>36</sup>A. I. Lavrentyev and S. Rokhlin, *J. Acoust. Soc. Am.* **103**, 657 (1998).
- <sup>37</sup>M. V. Golub and A. Boström, *Wave Motion* **48**, 105 (2011).
- <sup>38</sup>B. Gu, K. T. Nihei, and L. R. Myer, *J. Acoust. Soc. Am.* **102**, 120 (1997).
- <sup>39</sup>B. V. Derjaguin, V. M. Muller, and Y. P. Toporov, *J. Colloid Interface Sci.* **53**, 314 (1975).
- <sup>40</sup>L. J. Pyrak-Nolte and N. G. Cook, *Geophys. Res. Lett.* **14**, 1107, <https://doi.org/10.1029/GL014i011p01107> (1987).
- <sup>41</sup>J. Du, B. R. Tittmann, and H. S. Ju, *Thin Solid Films* **518**, 5786 (2010).
- <sup>42</sup>G. Tas, J. Loomis, H. Maris, A. Bailes Iii, and L. Seiberling, *Appl. Phys. Lett.* **72**, 2235 (1998).
- <sup>43</sup>T. Dehoux, O. B. Wright, R. L. Voti, and V. E. Gusev, *Phys. Rev. B* **80**, 235409 (2009a).
- <sup>44</sup>C. Thomsen, J. Strait, Z. Vardeny, H. J. Maris, J. Tauc, and J. Hauser, *Phys. Rev. Lett.* **53**, 989 (1984).
- <sup>45</sup>O. Matsuda, M. C. Larciprete, R. L. Voti, and O. B. Wright, *Ultrasonics* **56**, 3 (2015).
- <sup>46</sup>T. Dehoux, N. Chigarev, C. Rossignol, and B. Audoin, *Phys. Rev. B* **77**, 214307 (2008).
- <sup>47</sup>C. Rossignol, J.-M. Rampnoux, M. Pertot, B. Audoin, and S. Dilhaire, *Phys. Rev. Lett.* **94**, 166106 (2005).
- <sup>48</sup>T. Pezeril, C. Klieber, S. Andrieu, and K. Nelson, *Phys. Rev. Lett.* **102**, 107402 (2009).
- <sup>49</sup>O. Matsuda, K. Tsutsui, G. Vaudel, T. Pezeril, K. Fujita, and V. Gusev, *Phys. Rev. B* **101**, 224307 (2020).
- <sup>50</sup>A. Abbas, Y. Guillet, J.-M. Rampnoux, P. Rigail, E. Mottay, B. Audoin, and S. Dilhaire, *Opt. Express* **22**, 7831 (2014).
- <sup>51</sup>J. A. Rogers, A. A. Maznev, M. J. Banet, and K. A. Nelson, *Annu. Rev. Mater. Sci.* **30**, 117 (2000).
- <sup>52</sup>M. Hiraiwa, M. Abi Ghanem, S. P. Wallen, A. Khanolkar, A. A. Maznev, and N. Boechler, *Phys. Rev. Lett.* **116**, 198001 (2016).
- <sup>53</sup>J. Higuet, T. Valier-Brasier, T. Dehoux, and B. Audoin, *Rev. Sci. Instrum.* **82**, 114905 (2011).
- <sup>54</sup>M. Abi Ghanem, L. Khoryati, R. Behrou, A. Khanolkar, S. Raetz, F. Allein, N. Boechler, and T. Dehoux, *Appl. Mater. Today* **22**, 100934 (2021).
- <sup>55</sup>N. Chigarev, C. Rossignol, and B. Audoin, *Rev. Sci. Instrum.* **77**, 114901 (2006).
- <sup>56</sup>B. Perrin, B. Bonello, J. Jeannet, and E. Romatet, *Prog. Nat. Sci.* **6**, S444 (1996).
- <sup>57</sup>T. Tachizaki, T. Muroya, O. Matsuda, Y. Sugawara, D. H. Hurley, and O. B. Wright, *Rev. Sci. Instrum.* **77**, 043713 (2006).
- <sup>58</sup>M. Nikoonahad, S. Lee, and H. Wang, *Appl. Phys. Lett.* **76**, 514 (2000).
- <sup>59</sup>S. Mezil, F. Bruno, S. Raetz, J. Laurent, D. Royer, and C. Prada, *J. Acoust. Soc. Am.* **138**, 3202 (2015).
- <sup>60</sup>V. E. Gusev and P. Ruello, *Appl. Phys. Rev.* **5**, 031101 (2018).
- <sup>61</sup>F. Kargar and A. A. Balandin, *Nat. Photonics* **15**, 720 (2021).

- <sup>62</sup>B. Verstraeten, J. Sermeus, R. Salenbien, J. Fivez, G. Shkerdin, and C. Glorieux, *Photoacoustics* **3**, 64 (2015).
- <sup>63</sup>U. Choudhry, T. Kim, M. Adams, J. Ranasinghe, R. Yang, and B. Liao, *J. Appl. Phys.* **130**, 231101 (2021).
- <sup>64</sup>J. A. Rogers and K. A. Nelson, *J. Adhes.* **50**, 1 (1995).
- <sup>65</sup>S. Mezil, J. Laurent, D. Royer, and C. Prada, *Appl. Phys. Lett.* **105**, 021605 (2014).
- <sup>66</sup>R. Hodé, S. Raetz, J. Blondeau, N. Chigarev, N. Cuvillier, V. Tournat, and M. Ducousoo, *Appl. Phys. Lett.* **116**, 104101 (2020).
- <sup>67</sup>T. Valier-Brasier, T. Dehoux, and B. Audoin, *J. Appl. Phys.* **112**, 024904 (2012).
- <sup>68</sup>M. Robin, F. Jenot, M. Ouaftouh, and M. Duquennoy, *Ultrasonics* **102**, 106051 (2020).
- <sup>69</sup>D. Clorennec, C. Prada, D. Royer, and T. W. Murray, *Appl. Phys. Lett.* **89**, 024101 (2006).
- <sup>70</sup>C. Prada, O. Balogun, and T. Murray, *Appl. Phys. Lett.* **87**, 194109 (2005).
- <sup>71</sup>D. Clorennec, C. Prada, and D. Royer, *IEEE Trans. Ultrason. Ferroelectr. Freq. Controlled* **57**, 1125 (2010).
- <sup>72</sup>G. A. Antonelli, B. Perrin, B. C. Daly, and D. G. Cahill, *MRS Bull.* **31**, 607 (2006).
- <sup>73</sup>A. Y. Klokov, N. Y. Frolov, A. I. Sharkov, S. N. Nikolaev, M. A. Chernopitssky, S. I. Chentsov, M. V. Pugachev, A. I. Duleba, A. V. Shupletsov, V. S. Krivobok *et al.*, *Nano Lett.* **22**, 2070 (2022).
- <sup>74</sup>J. D. Greener, A. V. Akimov, V. Gusev, Z. Kudrynskyi, P. H. Beton, Z. D. Kovalyuk, T. Taniguchi, K. Watanabe, A. Kent, and A. Patané, *Phys. Rev. B* **98**, 075408 (2018).
- <sup>75</sup>M. Abi Ghanem, T. Dehoux, O. F. Zouani, A. Gadalla, M.-C. Durrieu, and B. Audoin, *J. Biophotonics* **7**, 453 (2014).
- <sup>76</sup>M. Abi Ghanem, T. Dehoux, L. Liu, G. L. Saux, L. Plawinski, M.-C. Durrieu, and B. Audoin, *Rev. Sci. Instrum.* **89**, 014901 (2018).
- <sup>77</sup>M. Grossmann, M. Schubert, C. He, D. Brick, E. Scheer, M. Hettich, V. Gusev, and T. Dekorsy, *New J. Phys.* **19**, 053019 (2017).
- <sup>78</sup>M. Hettich, A. Bruchhausen, S. Riedel, T. Geldhauser, D. Issenmann, O. Ristow, R. Chauhan, J. Dual, A. Erbe, E. Scheer *et al.*, *Appl. Phys. Lett.* **98**, 261908 (2011).
- <sup>79</sup>M. D. Losego, M. E. Grady, N. R. Sottos, D. G. Cahill, and P. V. Braun, *Nat. Mater.* **11**, 502 (2012).
- <sup>80</sup>T. G. Park, H. R. Na, S.-H. Chun, W. B. Cho, S. Lee, and F. Rotermund, *Nanoscale* **13**, 19264 (2021).
- <sup>81</sup>C. Li, A. V. Scherbakov, P. Soubelet, A. K. Samusev, C. Ruppert, N. Balakrishnan, V. E. Gusev, A. V. Stier, J. J. Finley, M. Bayer *et al.*, *Nano Lett.* **23**, 8186 (2023b).
- <sup>82</sup>P.-J. Wang, P.-C. Tsai, Z.-S. Yang, S.-Y. Lin, and C.-K. Sun, *Photoacoustics* **28**, 100412 (2022).
- <sup>83</sup>W. Yan, A. V. Akimov, M. Barra-Burillo, M. Bayer, J. Bradford, V. E. Gusev, L. E. Hueso, A. Kent, S. Kukhtaruk, A. Nadzeyka *et al.*, *Nano Lett.* **22**, 6509 (2022).
- <sup>84</sup>J. D. Greener, E. de Lima Savi, A. V. Akimov, S. Raetz, Z. Kudrynskyi, Z. D. Kovalyuk, N. Chigarev, A. Kent, A. Patané, and V. Gusev, *ACS Nano* **13**, 11530 (2019).
- <sup>85</sup>M. Lee, M. P. Robin, R. H. Guis, U. Filippozzi, D. H. Shin, T. C. Van Thiel, S. P. Paardekooper, J. R. Renshof, H. S. Van Der Zant, A. D. Caviglia *et al.*, *Nano Lett.* **22**, 1475 (2022).
- <sup>86</sup>R. Beardsley, A. V. Akimov, J. D. Greener, G. W. Mudd, S. Sandeep, Z. R. Kudrynskyi, Z. D. Kovalyuk, A. Patané, and A. J. Kent, *Sci. Rep.* **6**, 26970 (2016).
- <sup>87</sup>T. Dehoux, N. Tsapis, and B. Audoin, *Soft Matter* **8**, 2586 (2012).
- <sup>88</sup>K. L. Johnson, K. Kendall, and A. Roberts, *Proc. R. So. London Ser. A* **324**, 301 (1971).
- <sup>89</sup>T. Dehoux, M. Abi Ghanem, O. F. Zouani, M. Ducousoo, N. Chigarev, C. Rossignol, N. Tsapis, M.-C. Durrieu, and B. Audoin, *Ultrasonics* **56**, 160 (2015).
- <sup>90</sup>C. Jean, L. Belliard, T. W. Cornelius, O. Thomas, Y. Pennec, M. Cassinelli, M. E. Toimil-Molares, and B. Perrin, *Nano Lett.* **16**, 6592 (2016).
- <sup>91</sup>W.-S. Chang, F. Wen, D. Chakraborty, M.-N. Su, Y. Zhang, B. Shuang, P. Nordlander, J. E. Sader, N. J. Halas, and S. Link, *Nat. Commun.* **6**, 7022 (2015).
- <sup>92</sup>Y. Guillet, B. Audoin, M. Ferrié, and S. Ravaine, *Phys. Rev. B* **86**, 035456 (2012).
- <sup>93</sup>N. Del Fatti, C. Voisin, F. Chevy, F. Vallée, and C. Flytzanis, *J. Chem. Phys.* **110**, 11484 (1999).
- <sup>94</sup>T. Dehoux, T. Kelf, M. Tomoda, O. Matsuda, O. Wright, K. Ueno, Y. Nishijima, S. Juodkazis, H. Misawa, V. Tournat *et al.*, *Opt. Lett.* **34**, 3740 (2009b).
- <sup>95</sup>N. Vogel, M. Retsch, C.-A. Fustin, A. Del Campo, and U. Jonas, *Chem. Rev.* **115**, 6265 (2015).
- <sup>96</sup>N. Boechler, J. Eliason, A. Kumar, A. Maznev, K. Nelson, and N. Fang, *Phys. Rev. Lett.* **111**, 036103 (2013).
- <sup>97</sup>A. Khanolkar, S. Wallen, M. Abi Ghanem, J. Jenks, N. Vogel, and N. Boechler, *Appl. Phys. Lett.* **107**, 071903 (2015).
- <sup>98</sup>B. Graczykowski, N. Vogel, K. Bley, H.-J. Butt, and G. Fytas, *Nano Lett.* **20**, 1883 (2020).
- <sup>99</sup>S. P. Wallen, A. A. Maznev, and N. Boechler, *Phys. Rev. B* **92**, 174303 (2015).
- <sup>100</sup>P. H. Otsuka, S. Mezil, O. Matsuda, M. Tomoda, A. A. Maznev, T. Gan, N. Fang, N. Boechler, V. E. Gusev, and O. B. Wright, *New J. Phys.* **20**, 013026 (2018).
- <sup>101</sup>J. Eliason, A. Vega-Flick, M. Hiraiwa, A. Khanolkar, T. Gan, N. Boechler, N. Fang, K. Nelson, and A. Maznev, *Appl. Phys. Lett.* **108**, 061907 (2016).
- <sup>102</sup>A. Vega-Flick, R. Duncan, S. Wallen, N. Boechler, C. Stelling, M. Retsch, J. Alvarado-Gil, K. A. Nelson, and A. Maznev, *Phys. Rev. B* **96**, 024303 (2017).
- <sup>103</sup>M. Abi Ghanem, A. Khanolkar, H. Zhao, and N. Boechler, *Adv. Funct. Mater.* **30**, 1909217 (2020).
- <sup>104</sup>G. Pharr, W. C. Oliver, and F. Brotzen, *J. Mater. Res.* **7**, 613 (1992).
- <sup>105</sup>M. Abi Ghanem, A. Khanolkar, S. P. Wallen, M. Helwig, M. Hiraiwa, A. A. Maznev, N. Vogel, and N. Boechler, *Nanoscale* **11**, 5655 (2019).
- <sup>106</sup>M. Rey, T. Yu, R. Guenther, K. Bley, and N. Vogel, *Langmuir* **35**, 95 (2019).
- <sup>107</sup>A. Ayouch, X. Dieudonné, G. Vaudel, H. Piombini, K. Vallé, V. Gusev, P. Belleville, and P. Ruello, *Acsl Nano* **6**, 10614 (2012).
- <sup>108</sup>J. Avice, C. Boscher, G. Vaudel, G. Brotons, V. Juve, M. Edely, C. Méthivier, V. E. Gusev, P. Belleville, H. Piombini *et al.*, *J. Phys. Chem. C* **121**, 23769 (2017).
- <sup>109</sup>E. Alonso-Redondo, M. Schmitt, Z. Urbach, C. Hui, R. Sainidou, P. Rembert, K. Matyjaszewski, M. Bockstaller, and G. Fytas, *Nat. Commun.* **6**, 8309 (2015).
- <sup>110</sup>V. Babacic, J. Varghese, E. Coy, E. Kang, M. Pochylski, J. Gapinski, G. Fytas, and B. Graczykowski, *J. Colloid Interface Sci.* **579**, 786 (2020).
- <sup>111</sup>Q. Xie, S. Mezil, P. H. Otsuka, M. Tomoda, J. Laurent, O. Matsuda, Z. Shen, and O. B. Wright, *Nat. Commun.* **10**, 2228 (2019).
- <sup>112</sup>S. Mezil, N. Chigarev, V. Tournat, and V. Gusev, *Ultrasonics* **69**, 225 (2016).
- <sup>113</sup>A. Huynh, B. Perrin, and A. Lemaître, *Ultrasonics* **56**, 66 (2015).
- <sup>114</sup>L. Foglia, R. Mincigrucci, A. Maznev, G. Baldi, F. Capotondi, F. Caporaletti, R. Comin, D. De Angelis, R. Duncan, D. Fainozzi *et al.*, *Photoacoustics* **29**, 100453 (2023).
- <sup>115</sup>R. Delalande, D. Garcia-Sánchez, and L. Belliard, *Phys. Rev. B* **107**, 085409 (2023).
- <sup>116</sup>M. Tomoda, T. Dehoux, Y. Iwasaki, O. Matsuda, V. E. Gusev, and O. B. Wright, *Sci. Rep.* **4**, 4790 (2014).
- <sup>117</sup>R. Hodé, S. Raetz, N. Chigarev, J. Blondeau, N. Cuvillier, V. Gusev, M. Ducousoo, and V. Tournat, *J. Acoustical Soc. Am.* **150**, 2076 (2021).
- <sup>118</sup>F. Reverdy and B. Audoin, *J. Acoust. Soc. Am.* **109**, 1965 (2001a).
- <sup>119</sup>F. Reverdy and B. Audoin, *J. Appl. Phys.* **90**, 4829 (2001b).
- <sup>120</sup>J. Spytek, L. Ambrozinski, and I. Pelivanov, *Photoacoustics* **29**, 100440 (2023).
- <sup>121</sup>B. Lu, M. Abramchuk, F. Tafti, and D. H. Torchinsky, *JOSA B* **37**, 433 (2020).